RSC Advances

PAPER

View Article Online
View Journal | View Issue

Cite this: *RSC Adv.*, 2022, **12**, 2603

Highly dispersed NiS_2 quantum dots as a promising cocatalyst bridged by acetylene black significantly improved the photocatalytic H_2 evolution performance of g-C_3N_4 nanosheets

Miaomiao Li, * Qilin Pan, Mucang Xiao and Jianwen Xiong

In this work, ternary nanocomposite (CNs–AB/NiS_2) as a novel efficient H_2 evolution photocatalyst without the use of noble metals was successfully synthesized by depositing acetylene black (AB) and ultra-fine NiS_2 nanoparticles on the surface of CNs (g-C_3N_4) through ultrasonic dispersion and chemical vapor deposition methods, respectively. It was revealed that the loaded AB and NiS_2 nanoparticles have significantly improved the photocatalytic H_2 evolution efficiency of the CNs by improving the photogenerated electron–hole pair separation, visible light absorption and hydrogen evolution kinetics. Besides acting as a cocatalyst, AB served as a conductive electron bridge between CNs and NiS_2, which accelerated the effective transfer of electrons from CNs to NiS_2 and improved the H_2 evolution kinetics of the NiS_2 cocatalyst. The H_2 evolution experiments revealed that the ternary photocatalyst CNs–AB/$NiS_2$10 displayed a H_2 evolution rate of up to 2434.85 μmoL g^{-1} h^{-1}, which was a 1.41 times enhancement compared to that of the binary composite CNs–$NiS_2$10 and was 12.43 times higher than that of the pure CNs. Moreover, the ternary photocatalyst CNs–AB/$NiS_2$10 not only exhibited excellent photocatalytic activity and stability in the tests, but provided a novel idea for the development of high-efficiency catalysts free of noble metals as well.

Received 5th October 2021
Accepted 18th December 2021

DOI: 10.1039/d1ra07110f

rsc.li/rsc-advances

1 Introduction

In recent years, the energy crisis and environmental pollution have been major issues for human society.[1] Thus, it is highly desirable to search for and develop novel environmentally friendly and renewable energy sources. Hydrogen is widely recognized as the most promising alternative to fossil fuels due to its pollution-free combustion products and high energy density.[2–4] Among the strategies for H_2 production, photocatalytic water splitting is widely recognized as an effective and economical approach to produce hydrogen due to its sustainability and environmental friendliness.[5–8] However, no photocatalyst capable of producing hydrogen on a large scale with high efficiency, stability, safety and a low cost has been developed for H_2 evolution at present.[9] Therefore, it is essential to develop novel photocatalysts with high activity, low cost and good stability for efficient photocatalytic H_2 production. The two-dimensional layered material g-C_3N_4 is considered as an exciting material for water splitting due to its narrow band gap, chemical and thermal stability and excellent electronic properties.[10–13] Nevertheless, the photocatalytic performance of pure g-C_3N_4 is constrained by its fast charge recombination, low surface area and narrow light absorption range.[10,14] As a result, various modification methods have been investigated to overcome these weaknesses, like constructing heterojunctions, element doping, cocatalyst loading, morphoregulation and so on.[15–19] Among these strategies, cocatalyst loading, such as with transition and noble metals, to improve the charge separation efficiency and solar energy utilization of pure g-C_3N_4 is a particularly effective method.[4,20] In general, loading noble metals, such as Pt, Au and Ag, on pure photocatalysts can apparently promote the separation of photoexcited holes and electrons, increase the surface active sites and reduce the H_2 evolution overpotential of the photocatalyst.[17,21] However, their high price and low natural abundance have severely restricted the application of noble metals.[12,22] Transition metal sulfides (*e.g.*, CoS_x,[23] CuS_x,[24] MoS_2,[25,26] WS_2 [27] and CdS [28,29]) have been widely used as H_2 evolution promoters in the electrocatalytic field due to their stability, low overpotential, low cost and excellent activity,[30] which indicates that transition metal sulfides may be promising cocatalysts for photocatalytic H_2 evolution.[31–33] Zhu *et al.*,[6] Fie *et al.*,[34] and Li *et al.*[35] have reported NiS_2 as a cocatalyst in the photocatalytic HER. However, the NiS_2 cocatalysts prepared by the hydrothermal method in these reports are of poor dispersibility and suffer from serious agglomeration; there are also potential safety hazards in the preparation process. Furthermore,

School of Physics and Telecommunication Engineering, South China Normal University, Guangzhou, 510631, Guangdong, China. E-mail: jwxiong@scnu.edu.cn; Tel: +86 020 85216860

the agglomerated nanoparticles can easily become the recombination center of photogenerated carriers, which could reduce the migration and separation carriers, so as to restrict the improvement of the photocatalytic efficiency.[6,36] Based on the above, we developed a new preparation method to deposit ultrafine and highly dispersed NiS_2 nanoparticles on the CNs surface. Ultra-fine and highly dispersed NiS_2 nanoparticles synthesized by a chemical vapor deposition method could provide more reactive active sites for the HER, promote the separation and migration of carriers and improve the photocatalytic performance of g-C_3N_4 nanosheets. However, compared to noble metals, NiS_2 possesses a weaker conductivity and a lower work function, which means poor collection and utilization of photogenerated electrons compared to those of noble metals. Acetylene black (AB) is widely used as a common conductive additive, which can remarkably improve the photocatalytic efficiency by accelerating the transfer and diffusion of electrons (or holes) on the surface of the catalyst and reducing the recombination rate of electron–hole pairs on the interface of the photocatalyst owing to its excellent conductivity and stability.[37,38]

In this work, we creatively reported noble metal-free NiS_2 and AB co-modified g-C_3N_4 nanosheets (CNs–AB/NiS_2) as a promising photocatalyst for water splitting. The synergy between NiS_2 cocatalyst and conductive layer AB can significantly improve the photocatalytic HER performance by improving the photogenerated electron–hole pair separation, visible light absorption and hydrogen evolution kinetics. Specifically, under the irradiation of visible light, the conductive AB layer deposited on the surface of the CNs served as an electron bridge to promote the diffusion and transfer of in-plane charges, while the highly dispersed NiS_2 nanoparticles effectively improved the light absorption capacity of the CNs, accelerated the effective separation and migration of photoexcited carriers, provided abundant active sites for the hydrogen evolution reaction (HER) and further improved the photocatalytic efficiency of the CNs as shown in Fig. 1.[11,38] The photocatalytic H_2 evolution rate of the ternary photocatalyst CNsAB/$NiS_2$10 boosted to 2434.85 μmoL h^{-1} g^{-1}, which is 12.43 times higher than that of the CNs and is much higher than that of the photocatalysts in previous reports.[39–41] All in all, this study has provided a new strategy for the design and synthesis of efficient, stable and non-noble metal based systems for photocatalytic H_2 evolution.

2 Experimental

2.1 Materials

Thiourea (CH_4N_2S), urea ($CO(NH)_2$) and absolute ethanol were supplied by Guangzhou Chemical Reagent Co., Ltd. (Guangzhou, China). Ammonium bicarbonate (NH_4HCO_3) was obtained from Damao chemical Reagent industry Co., Ltd. (Tianjin, China). Acetylene black powder (AB) was purchased from Yingshida graphite Co., Ltd. (Qingdao, China). Nickel chloride hexahydrate ($NiCl_2 \cdot 6H_2O$) and triethanolamine (TEOA) were purchased from Shanghai Macklin Biochemical Co., Ltd. (Shanghai, China). All chemicals were of analytical grade and were used as purchased.

2.2 Synthesis of the g-C_3N_4 nanosheets (CNs)

The g-C_3N_4 nanosheets were synthesized according to previous literature.[5] Specifically, 4 g of urea in a crucible was heated to 550 °C for 4 h with a ramping rate of 2.5 °C min^{-1}. Then, it was heated at 500 °C for an additional 2 h. Afterwards, the residual yellow power was collected, washed with deionized water and dried in a vacuum freeze oven for 10 h. Ultra-thin g-C_3N_4 nanosheets (CNs) were obtained.

2.3 Synthesis of the CNs–AB composite

1 g of the as prepared CNs and 5 mg AB were dispersed into 50 mL of absolute ethanol with vigorous stirring for 1 h, the

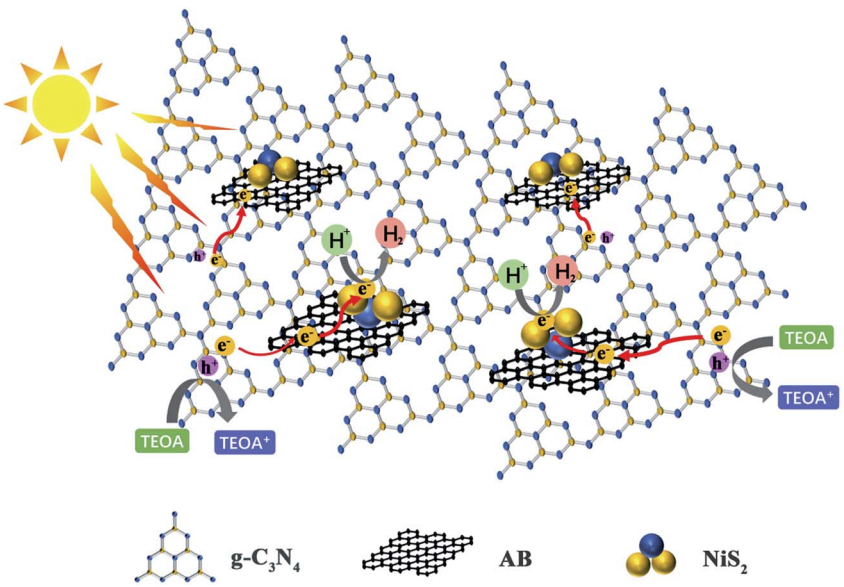

Fig. 1 Photocatalytic H_2 evolution mechanism on the CNs–AB/NiS_2 composites.

obtained suspension was ultrasonicated for another 3 h. Afterwards, the resulting product was collected by filtering and dried in a vacuum oven for about 12 h at 60 °C. Finally, the CNs–AB composite was obtained and the quantity of AB loaded on the CNs was the optimal proportion, determined according to previous literature.[11,42]

2.4 Synthesis of the CNs–AB/$Ni_2(OH)_2 \cdot CO_3 \cdot 4H_2O$ composite

1 g CNs–AB and 0.0968 g $NiCl_2 \cdot 6H_2O$ (0.407 mmoL) were dissolved in 150 mL of absolute alcohol under magnetic stirring. After approximately 2 h, 0.0966 g NH_4HCO_3 (1.22 mmoL) was added into the mixed solution and stirred for another 6 h. Then, the obtained powder was washed with absolute alcohol 5 times, collected by centrifugation and dried at 60 °C overnight. The CNs–AB/$Ni_2(OH)_2 \cdot CO_3 \cdot 4H_2O$ composite was obtained.

2.5 Synthesis of the CNs–AB/NiS_2 composite

The as prepared nanocomposite CNs–AB/$Ni_2(OH)_2 \cdot CO_3 \cdot 4H_2O$ and the sulfur source CH_4N_2S in porcelain crucibles were placed at the air outlet and inlet of a tube furnace, respectively. Subsequently, the samples were heated at 350 °C for 2 hours with a ramping rate of 2 °C min^{-1} in an argon atmosphere. Ultra-thin g-C_3N_4 nanosheets dropping with 0.5 wt% AB and 5 wt% NiS_2 were obtained after cooling to room temperature and were denoted as CNs–AB/$NiS_2$5. CNs–AB compounds containing 10 wt% and 15 wt% nickel sulfide were prepared using the same approach and were called CNs–AB/$NiS_2$10 and CNs–AB/$NiS_2$15, respectively. g-C_3N_4 nanosheets containing 5 wt%, 10 wt% and 15 wt% NiS_2 were synthesized as well.

2.6 Characterization

The morphologies of the products were observed using scanning electron microscopy (JEOL JSM-6330F) and field emission transmission electron microscopy (JEOL-2100) at an accelerated voltage of 200 kV. XRD (X-ray diffraction) patterns of the CNs–AB/NiS_2 were obtained using a D/MAX 2500 V diffractometer with Cu-Kα radiation at 40 kV. UV-vis diffuse reflection spectroscopy was performed using a Shimadzu UV-2600 spectrophotometer with barium sulfate ($BaSO_4$) as the reference. An AXIS SUPRA surface analysis system was applied to record the X-ray photoelectron spectroscopy (XPS) with a C 1s peak at 284.8 eV as the internal standard. The photoluminescence (PL) spectra were recorded with a fluorescence spectrometer (Hitachi F-7000, Japan) with an excitation wavelength of 390 nm. Nitrogen adsorption–desorption studies, including the BET surface area and pore size distribution of the samples, were carried out on a JW-BK200C analyzer. Electrochemical tests were performed on a CHI 660E instrument in a three-electrode battery system. A Pt wire and Ag/AgCl electrode were used as the counter electrode and reference electrode, respectively. Na_2SO_4 aqueous solution (0.1 M) was used as the electrolyte. The apparent quantum efficiency (AQE) of the catalyst was measured using a xenon lamp (300 W) with a 400 ± 5 nm band-pass filter.

2.7 Photocatalytic H_2 evolution

Photocatalytic tests were performed on a photocatalytic water splitting hydrogen production system. Generally, 10 mg of CNs–AB/NiS_2 powder was dispersed in a Pyrex glass cell containing a mixed solution of 100 mL of water and 20 mL of TEOA (sacrificial agents) with a magnetic stirrer. The reaction system was in a vacuum state before the irradiation and the temperature of the system was maintained at 40 ± 0.5 °C. Subsequently, the reactor was exposed to a Xe lamp source with a filter ($\lambda > 420$ nm) for 4 h, the mixed solution was under magnetic stirring throughout the experiment to keep the photocatalyst in suspension all the time. The evolved H_2 was detected and collected using an online gas chromatograph with N_2 as the carrier gas during the process.

3 Results and discussion

The morphology and surface microstructure of the CNs, CNs–AB and CNs–AB/$NiS_2$10 were revealed using SEM and TEM. The SEM images of the CNs in Fig. 2A and D display a wrinkled, ultra-thin, flower-like nanoscale two-dimensional structure. The TEM images of the pure CNs–AB (Fig. 2B and E) reveal the shape of the CNs–AB. It is apparent that the AB nanoparticles were attached to the surface of the CNs, and the CNs–AB inherited the sheet-like morphology of the CNs well. However, for CNs–AB/$NiS_2$10, the NiS_2 nanoparticles can not be well distinguished from the AB nanoparticles in the TEM images (Fig. 2C and F), owing to the similar morphology of AB and NiS_2, and therefore EDX was used to detect the presence of NiS_2. Fig. 2G presents the mapping of CNs–AB/$NiS_2$10, and the brighter areas represent the higher concentration of the corresponding element in the patterns. It is obvious that C, N, Ni and S were highly dispersed on the surface of the composite in the elemental mapping images of CNs–AB/$NiS_2$10, which further

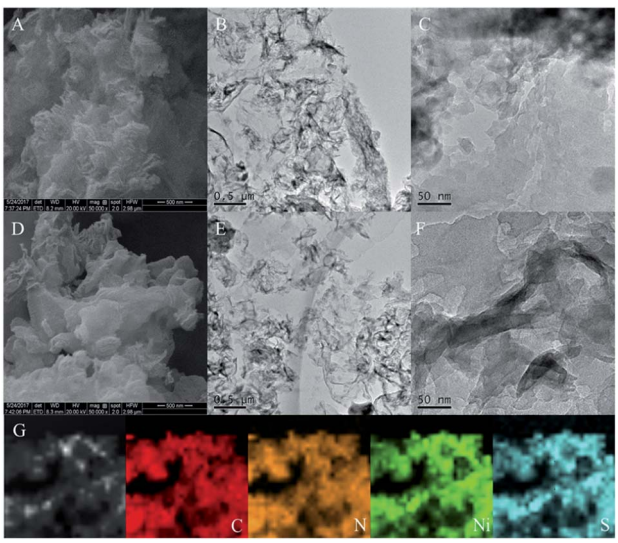

Fig. 2 SEM images of the CNs (A and D), TEM images of the CNs–AB (B and E) and CNs–AB/$NiS_2$10 (C and F) and the mapping of CNs–AB/$NiS_2$10 (G).

identified the successful synthesis of the CNs–AB/$NiS_2$10 composite material. The phase structures and compositions of the as-prepared CNs–AB/NiS_2 composites and pure CNs photocatalysts were analyzed using X-ray diffraction (XRD). Fig. 3A depicts the XRD patterns of the pure CNs and CNs–AB/NiS_2 composites with different amounts of NiS_2. As is shown in Fig. 3A, all of the samples featured two distinct characteristic peaks at 13.3° and 27.6°, which indicated the successful synthesis of g-C_3N_4 (JCPDS no. 87-1526).[11] The weaker diffraction peak at 13.3° corresponds to the in-plane structural packing pattern of the heptazine network and can be indexed as the (100) crystal plane of g-C_3N_4.[35,43] Another stronger diffraction peak at 27.6° can be designated as the interlayer stacking of the aromatic segments, which can be attributed to the (002) plane of g-C_3N_4.[44,45] The remaining series of weak peaks are attributed to NiS_2. Specifically, the peaks can be clearly identified at 31.4°, 35.3°, 45.1°, 48.0° and 53.4°, which matches well with NiS_2 (JCPDS no. 89-1495).[39,46] Furthermore, no diffraction peak for AB was observed in the nanocomposites, which is probably due to the low content and crystallinity of AB and its high dispersion on the surface of the CNs.[14] In addition, no shift of the diffraction peak of g-C_3N_4 was observed, indicating that the AB and NiS_2 nanoparticles loaded on the CNs did not changed the morphological structure of the CNs. From the above results, we found that the NiS_2 nanoparticles were successfully modified on the surface of the CNs–AB. The surface elemental composition analysis of CNs–AB/$NiS_2$10 was performed using X-ray photoelectron spectroscopy (XPS). As is

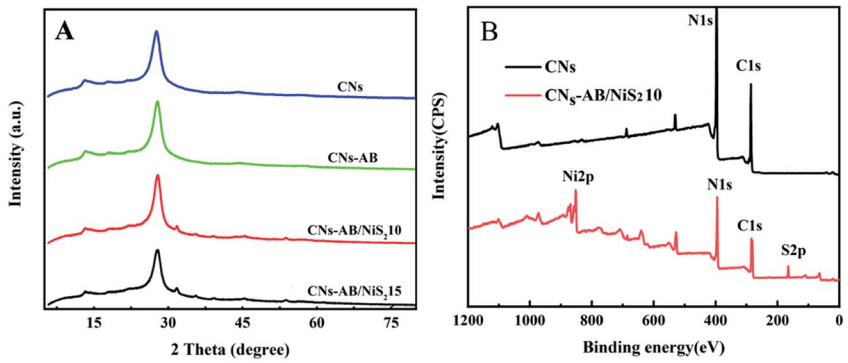

Fig. 3 XRD patterns of the CNs, CNs–AB, CNs–AB/$NiS_2$10 and CNs–AB/$NiS_2$15 composites (A). XPS survey spectra of the CNs and CNs–AB/$NiS_2$10 composites (B).

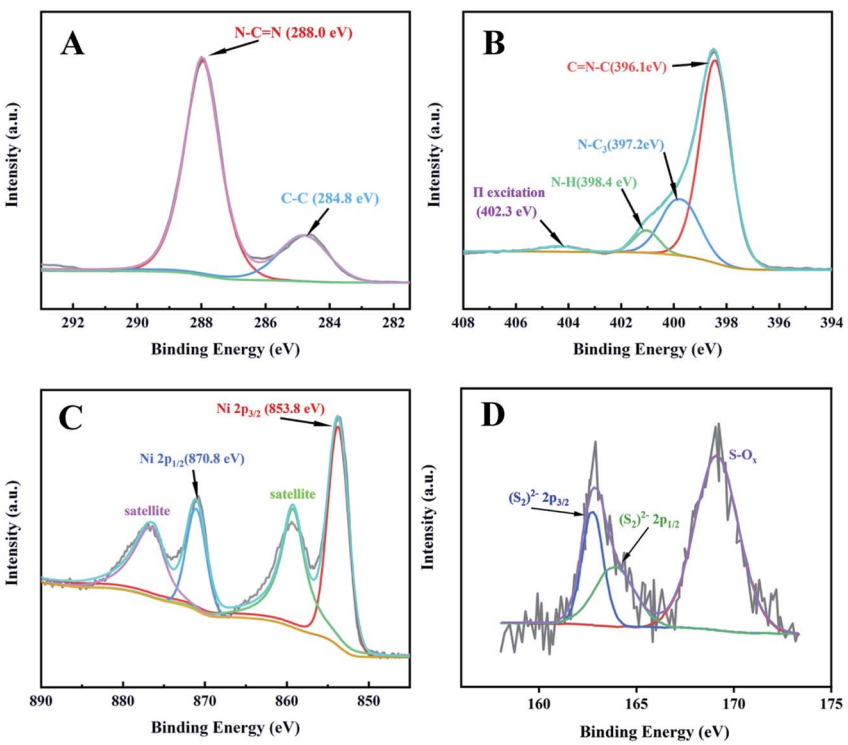

Fig. 4 High-resolution XPS spectra of C 1s (A), N 1s (B), Ni 2p (C) and S 2p (D).

depicted in the full XPS spectra of CNs–AB/$NiS_2$10 in Fig. 3B, CNs–AB/$NiS_2$10 contains C, N, S, and Ni elements. The high-resolution XPS spectrum of C 1s (Fig. 4A) showed two peaks. The first peak, with a binding energy of 284.8 eV, is assigned to AB (C–C bonding) adsorbed on the surface of CNs–AB/$NiS_2$10.[47] The peak at 288.0 eV was attributed to the characteristic graphite sp^2-hybridized carbon (N–C=N) in the g-C_3N_4 lattice.[48] Furthermore, the N 1s spectrum (Fig. 4B) consists of four peaks centered at 396.1 eV, 397.2 eV, 398.4 eV and 402.3 eV, ascribed to the binding energy of C–N=C (sp^2-hybridized nitrogen), N-C_3 (sp^3 tertiary nitrogen groups) and C–NH (amine groups) in and out of triazine rings and π-excitations, respectively.[39,42,49] The high-resolution spectrum of Ni 2p (Fig. 4C) could be deconvoluted into four peaks, which at 853.8 eV and 870.8 eV are corresponding to the Ni $2p^{3/2}$ and Ni $2p^{1/2}$ of Ni^{2+}, respectively.[34,50] The other two peaks with lower binding energies of 859.6 eV and 876.9 eV correspond to the satellite peaks. In terms of the S 2p spectrum (Fig. 4D), the XPS peak can be divided into two main peaks centered at 162.8 eV and 164.1 eV, which correspond to the typical $(S_2)^{2-}$ peaks, while the peak at 169.2 eV could be assigned to the S–O bonding due to the slight oxidation.[35,45,51] The above XPS results have further confirmed the synthesis of CNs–AB/$NiS_2$10.

UV-vis diffuse reflectance spectroscopy was used to study the optical properties of the photocatalysts. As shown in Fig. 5A, the CNs show a strong absorption band with an absorption edge at 450 nm, corresponding to a band gap of 2.75 eV. However, CNs–AB/$NiS_2$10 and CNs–AB/$NiS_2$15 exhibited a significantly stronger visible light absorption intensity compared to that of the CNs in the wavelength region above 450 nm. In addition, the absorption edges of the bands of CNs–AB/$NiS_2$10 and CNs–AB/$NiS_2$15 were slightly shifted to the longer wavelength direction. Based on the tangent of the $(\alpha\hbar\nu)^{1/2}$ to $\hbar\nu$ curve in Fig. 5B, the Kubelka–Munk method was used to estimate the band gap energy of the n-type CN photocatalyst (α and $\hbar\nu$ are the light absorption coefficient and photon energy, respectively).[52] The band gap of NiS_2 is 0.3 eV, which means a wide range of visible light absorption. Fig. 5B shows that the band gaps of CNs–AB/$NiS_2$15 and CNs–AB/$NiS_2$10 reduced to 2.72 eV and 2.73 eV, respectively, after loading NiS_2 and AB. As is known, a narrow band gap means a wider range of light absorption, which is beneficial to the improvement of photocatalytic efficiency. In brief, the significantly improved light absorption and narrow band gaps of CNs–AB/$NiS_2$10 and CNs–AB/$NiS_2$15 can boost the H_2 production activity.[53]

To explore the effect of AB and NiS_2 deposited on the CNs, the surface area and pore size distributions of the composites were characterized using nitrogen adsorption–desorption isotherms. It can be seen from Fig. 5C and D that the isotherms of both the CNs and CNs–AB/$NiS_2$10 display typical IV isotherm curves, indicating the mesoporous structural characteristics of the CNs and CNs–AB/$NiS_2$10.[9,54] In comparison with that of the CNs, the BET surface area of CNs–AB/$NiS_2$10 was increased to 77.1 $m^2\ g^{-1}$ from 69.3 $m^2\ g^{-1}$, revealing the increase of active sites on the CNs–AB/$NiS_2$10 surface. In addition, the higher surface area and larger pore volume of CNs–AB/$NiS_2$10 have not

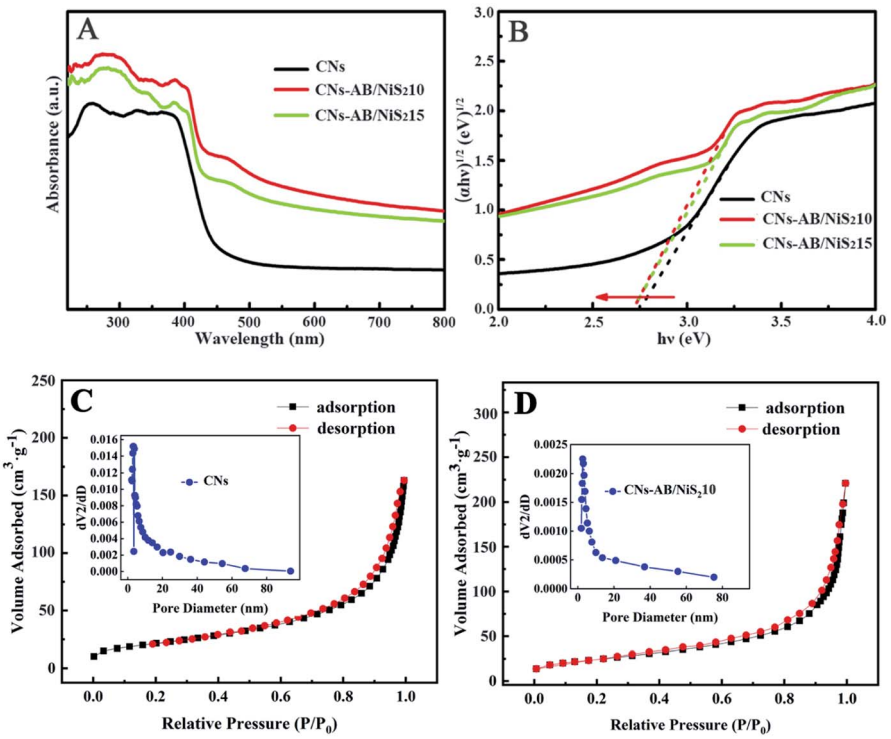

Fig. 5 UV-vis diffuse reflectance spectra of the CNs and CNs–AB/NiS_2 composites (A). Plot of $(\alpha\hbar\nu)^{1/2}$ *versus* $\hbar\nu$ for the band gap energy of the CNs and CNs–AB/NiS_2 composites (B). Nitrogen adsorption–desorption isotherms and pore size distribution of the CNs (C) and CNs–AB/$NiS_2$10 (D).

only accelerated the diffusion and transfer of the carriers, but also boosted the reflection of light in the pores, thereby improving the photocatalytic efficiency.[6,51]

Photocatalytic water splitting experiments were carried out under Xe lamp irradiation ($\lambda > 400$ nm) to evaluate the photocatalytic H_2 evolution of the CNs–AB/NiS_2 and CNs–NiS_2 composites, with 20% volume TEOA as a carrier sacrificial agent. For comparison, the average H_2 evolution rates of the CNs and CNs–AB/NiS_2 under visible light irradiation are depicted in Fig. 6A. It can be seen that, within 4 h of irradiation, the amount of H_2 produced on the pure CNs, CNs–AB, CNs–AB/$NiS_2$5, CNs–AB/$NiS_2$15 and CNs–AB/$NiS_2$10 photocatalysts were 725.05 μmoL g^{-1} h^{-1}, 1582.13 μmoL g^{-1} h^{-1}, 6611.92 μmoL g^{-1} h^{-1}, 7662.31 μmoL g^{-1} h^{-1} and 9739.43 μmoL g^{-1} h^{-1}, respectively. The H_2 evolution rate of CNs–AB/$NiS_2$10 reached 2434.85 μ moL g^{-1} h^{-1}, which is 12.43 times higher than that of the pure CNs. Moreover, the amount of H_2 released over all the photocatalysts increased linearly during the reaction, showing that all of the photocatalysts exhibit a favorable stability under visible light irradiation. Furthermore, it can be observed from Fig. 6A that the photocatalysts loaded with NiS_2 and AB exhibited a remarkably enhanced activity for H_2 evolution compared to that of the CNs. At the same time, the photocatalytic activity of the samples loaded with the same dose of NiS_2, but without AB (CNs–NiS_2) and CNs–AB, are demonstrated in Fig. 6B. It is clear that the binary photocatalysts exhibit a lower H_2 evolution rate compared to that of the ternary ones, revealing that the ternary photocatalyst CNs–AB/NiS_2 possessed a stronger photocatalytic activity compared to that of the binary composite CNs–NiS_2, since AB as a conductive bridge can greatly accelerate the separation of the photoexcited electrons and holes to enhance the photocatalytic performance of the CNs. Nevertheless, it is also apparent that CNs–AB/$NiS_2$15 produced less H_2 than CNs–AB/$NiS_2$10 during this process, which could be attributed to the shielding effect on the surface of the CNs caused by the excessive NiS_2 nanoparticles.[22,55,56]

In addition, compared to the previous literature, the hydrogen production of CNs–AB/$NiS_2$10 within 4 hours is about 520 times that of $Pt_{2.5}Co$/g-C_3N_4, 110 times that of g-C_3N_4 inverse opal photocatalysts, 380 times that of g-C_3N_4 with nitrogen vacancies and 1.11 times that of g-C_3N_4/Ti_3C_2 MXene.[57–60]

Considering the stability of a photocatalyst is a key factor for practical applications, cycling photocatalytic testing for H_2 evolution was implemented to evaluate the stability of the CNs–AB/$NiS_2$10 composite. As revealed in Fig. 6C, there was no evident decrease in the photocatalytic activity of the composites observed after six cycles of the photocatalytic reaction. It can be inferred that the ternary photocatalyst CNs–AB/$NiS_2$10 possesses excellent H_2 evolution stability and durability.

Besides the light absorption properties, the carrier dynamics of the samples have a great impact on the photocatalytic performance. The separation, migration and recombination of photoexcited charges were revealed by PL, transient photocurrent responses and electrochemical impedance spectra (EIS).[34] PL spectra were used to evaluate the separation efficiency of the photogenerated carriers.[9] As shown in Fig. 6D, the CNs showed a strong intrinsic emission peak at 420 nm, indicating a high recombination rate of the photoexcited charge carriers in the CNs, while the PL intensity of CNs–AB/$NiS_2$5, CNs–AB/$NiS_2$10, CNs–AB/$NiS_2$15 and CNs–$NiS_2$10 showed a slight blue shift and a significant decrease. The emission peak intensity of the samples decreased remarkably with the increase in the amounts of NiS_2, which indicated that the NiS_2 and AB nanoparticles

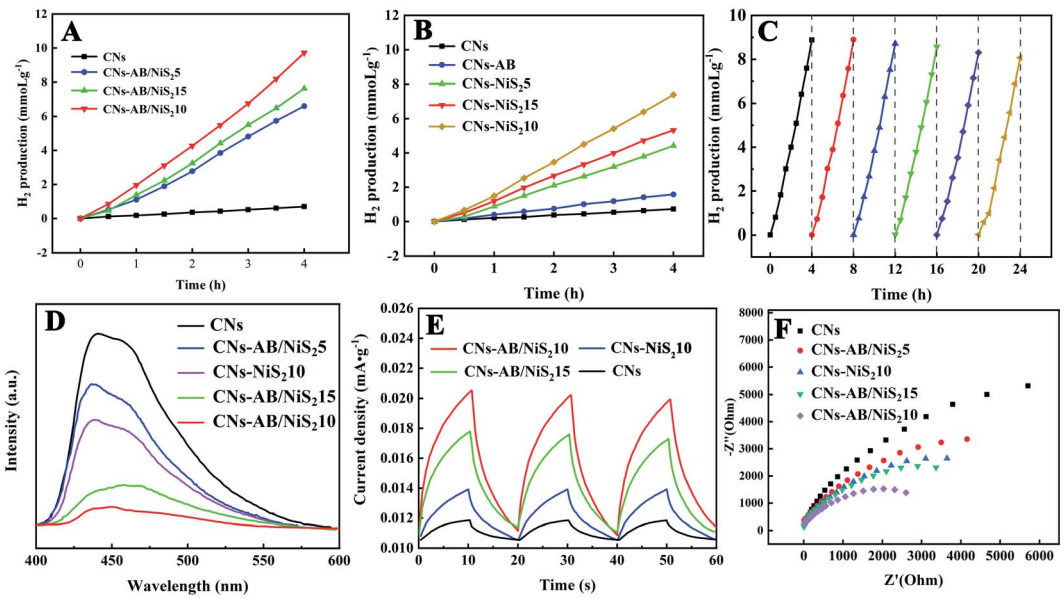

Fig. 6 Photocatalytic H_2 evolution with respect to time over different samples (A and B). Repeated cycles of photocatalytic H_2 evolution on CNs–AB/$NiS_2$10 (C). Steady-state photoluminescence spectra (D), transient photocurrent responses (E) and electrochemical impedance spectroscopy (F) of the samples.

loaded on the surface of the CNs greatly inhibited the recombination of the photoexcited electron–hole pairs, which was favorable to the photocatalytic HER.[61] In addition, the peak of the CNs–AB/NiS_2 was much lower than that of CNs–$NiS_2$10 as the PL spectra shows, indicating that AB served as an electron transfer bridge and accelerated the electron transfer from the CNs to the NiS_2 and markedly reduced the recombination rate of the electron–hole pairs.[31]

Transient photocurrent measurements were carried out to further study the rapid charge separation and transfer at the interface. Fig. 6E shows the rapid and reproducible photocurrent response of all the samples under intermittent visible light irradiation. The photocurrent response of the CNs increased with the loads of AB and NiS_2, indicating that the co-catalysts AB and NiS_2 effectively enhanced the interfacial charge separation and transfer of the CNs.[41,62] More importantly, the ternary photocatalyst CNs–AB/$NiS_2$10 exhibits the highest photocurrent density among all the photocatalysts, which reveals that the photoexcited carriers in CNs–AB/$NiS_2$10 can more easily separate and migrate to the surface of the CNs,[63] further indicating that the co-loading of AB and NiS_2 initiates the best charge separation and transfer, thus resulting in the highest photocatalytic H_2 evolution performance.[31,42] However, the photocurrent density of CNs–AB/$NiS_2$15 is slightly lower than that of CNs–AB/$NiS_2$10, which may be due to the excessive load of NiS_2.[53] On the one hand, the overloading of NiS_2 on the CNs may cause a shielding effect and reduce the absorption of incident light.[64,65] On the other hand, excess NiS_2 nanoparticles will become the recombination centers of photoexcited carriers.[66] Therefore, an appropriate amount of NiS_2 can effectively improve the activity of the photocatalyst, which provides a reference for the loading amount of the cocatalyst.[67]

EIS experiments were carried out to further confirm the enhanced interfacial charge separation. Nyquist plots of all the samples displayed semicircles in the middle frequency region, as shown in Fig. 6F, and the radius of the arcs are positively correlated with the electron transfer impedance (R_{et}).[31,68] The radii of the CNs loaded with different amounts of NiS_2 and AB are much smaller than that of the pure CNs on the Nyquist plots, descending in the following order: CNs > CNs–AB/$NiS_2$5 > CNs–$NiS_2$10 > CNs–AB/$NiS_2$15 > CNs–AB/$NiS_2$10, suggesting that the AB and NiS_2 loading can effectively reduce the charge transfer resistance of the CNs and improve the separation and transfer rate of the photoexcited electron–hole pairs.[69] Obviously, AB and NiS_2 on the surfaces of the CNs may accelerate the transfer and separation of charge and cause a slower recombination rate of the photoexcited electron–hole pairs, leading to a significant improvement in the photocatalytic H_2 evolution activity of the CNs. In addition, the ternary photocatalyst CNs–AB/$NiS_2$10 was observed to exhibit a smaller arc radius than that of CNs–$NiS_2$10, which was consistent with the result of the H_2 evolution tests, further confirming the prominent role of AB in improving the charge separation and transfer.

Fig. 7 shows the AQE of the CNs–AB/$NiS_2$10 sample at different irradiation wavelengths. The AQE value of the CNs–AB/$NiS_2$10 sample at 400 nm reached 4.12%, which indicated that the introduction of the NiS_2 and AB significantly improved the light absorption properties of the CNs and widened the light response intensity in the visible light region.[70,71]

Besides the wider range of light absorption, the enhanced photocatalytic activity of the ternary photocatalyst was mainly attributed to the effective separation and transfer of electrons and holes at the CNs interface from the above analysis.[12] The CNs without cocatalysts exhibit a low photocatalytic activity as a result of the rapid recombination of the photoexcited electrons from the conduction band (CB) and holes from the valence band (VB) under irradiation. After coupling with the NiS_2 and AB, the electrons in the valence band of the CNs were

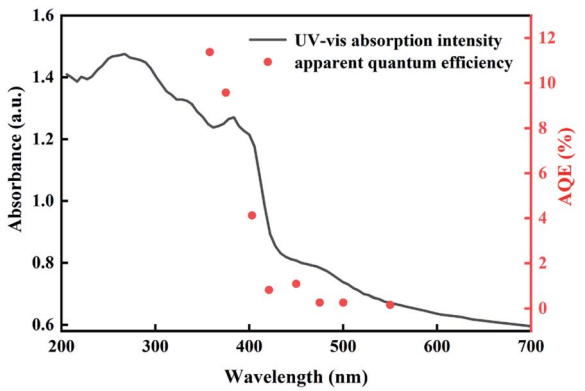

Fig. 7 Wavelength dependence of the AQE of CNs–AB/$NiS_2$10 for H_2 evolution (right axis) and UV-vis absorption spectrum of CNs–AB/$NiS_2$10 (left axis).

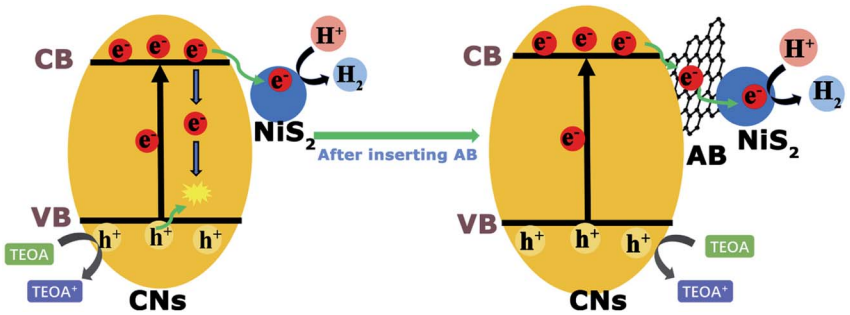

Fig. 8 Proposed mechanisms of the photoexcited charge transfer over the CNs–NiS_2 and CNs–AB/NiS_2.

excited to the conduction band, then the excitation electrons could be quickly migrated to the CB of the NiS_2 by AB under irradiation.[51] At the same time, the remaining photoexcited holes in the valence band of the CNs were rapidly quenched by the TEOA sacrificial agent. In this way, the photoexcited electrons and holes can be effectively separated as is proposed in Fig. 8, and the electrons that migrated to the NiS_2 would react with the H^+ in the solution to generate H_2.[35,72] Therefore, the CNs–AB/NiS_2 exhibited a preferable photocatalytic performance in the photocatalytic H_2 reaction than the binary photocatalysts CNs–NiS_2 and the pure CNs. On the other hand, the highly dispersed NiS_2 as a cocatalyst significantly increased the active sites on the CNs surface. However, a shielding effect will work when the content of NiS_2 was further increased above the optimal value, resulting in a decrease in the photocatalytic performance. As a result, the as-prepared CNs–AB/NiS_2 composites exhibit an excellent photocatalytic H_2 evolution performance, which can be attributed to the synergistic effect of the AB and NiS_2, thereby significantly increasing the photoresponse range of the CNs, improving the separation efficiency of the photoexcited electrons and holes, and increasing the specific surface area of CNs.

4 Conclusions

In conclusion, we have successfully designed and synthesised a series of binary and ternary photocatalysts by dispersing NiS_2 or/and AB nanoparticles on ultra-thin g-C_3N_4 nanosheets as excellent photocatalysts, without a noble metal cocatalyst, for H_2 generation using a novel approach. Specifically, the AB nanoparticles at the interface act as an effective bridge to accelerate the transfer of photoexcited electrons from the CNs to the NiS_2. The NiS_2 cocatalyst, with excellent dispersibility, has provided more active sites for the HER. The co-modification of AB and NiS_2 not only resulted in a significant increase of the specific surface area and light absorption range of the CNs, but significantly boosted the separation and transfer of the electrons at the interface of the catalyst and reduced the recombination rate of the carriers. All in all, the cocatalyst AB and NiS_2 nanoparticles have remarkably improved the photocatalytic performance of the CNs, therefore the ternary photocatalyst CNs–AB/$NiS_2$10 exhibits the highest H_2 generation rate of 2434.85 μmoL h^{-1} g^{-1} under visible light irradiation, which is 12.43 times higher than that of the CNs. Moreover, cyclic hydrogen evolution tests proved that the ternary photocatalyst was stable enough for practical applications. This work provides a new route for the design and development of noble metal-free photocatalysts with excellent properties; we hope that this leads to the development of more and more strategies to improve the efficiency of photocatalytic hydrogen production.

Conflicts of interest

There are no conflicts to declare.

Acknowledgements

This work has been financially supported by the National Natural Science Foundation of China (61072029), the Natural Science Foundation of Guangdong Province, China (10151063101000025) and the Science and Technology Planning Project of Guangzhou City, China (2010Y1-C111).

Notes and references

1 X. Feng, B. Lv, L. Lu, X. Feng, H. Wang, B. Xu, Y. Yang and F. Zhang, *Appl. Surf. Sci.*, 2021, **562**, 150106.
2 W. A. Yan, B. Dwa, B. Hla, J. Wei, B. Tza, D. A. Xu, H. A. Bo, B. Cla and B. Gca, *Appl. Surf. Sci.*, 2021, **567**, 150903.
3 J. Zhang, W. Hu, S. Cao and L. Piao, *Nano Res.*, 2020, **13**, 2313–2322.
4 D. Zeng, W. Xu, W. J. Ong, J. Xu, H. Ren, Y. Chen, H. Zheng and D. L. Peng, *Appl. Catal., B*, 2018, **221**, 47–55.
5 H. Yang, R. Cao, P. Sun, J. Yin and S. Zhang, *Appl. Catal., B*, 2019, **256**, 117862.
6 C. Zhu, Z. Jiang, W. Wei, L. Chen, D. Liu, K. Qian, X. Lü and J. Xie, *Res. Chem. Intermed.*, 2016, **42**, 6483–6499.
7 W. Liu, R. Peng, X. Ye, J. Guo and L. Luo, *Appl. Surf. Sci.*, 2021, **560**, 150013.
8 C. Lu, E. Wu, C. Li, W. Dou, Y. Lian, Y. Liang, X. Xiang and H. Wang, *J. Phys. Chem. Solids*, 2021, **158**, 110228.
9 J. Feng, J. Bian, L. Bai, S. Xi, Y. Wang, C. Chen and L. Jing, *Appl. Catal., B*, 2021, **295**, 120260.
10 F. He, M. Wang, L. Luo, Z. Wang and Y. Li, *Appl. Surf. Sci.*, 2021, **562**, 150103.
11 J. Wen, J. Xie, Z. Yang, R. Shen and L. Xin, *ACS Sustainable Chem. Eng.*, 2017, **5**, 3.
12 Y. Liang, W. Xu, J. Fang, Z. Liu and Z. Fang, *Appl. Catal., B*, 2021, **295**, 120279.
13 H. Mou, J. Wang, D. Yu, D. Zhang, W. Chen, Y. Wang, D. Wang and T. Mu, *ACS Appl. Mater. Interfaces*, 2019, **11**, 44360–44365.
14 W. Tan, Y. Li, W. Jiang, C. Gao and C. Zhuang, *ACS Appl. Energy Mater.*, 2020, **3**, 8048–8054.
15 C. Liu, Y. Feng, Z. Han, Y. Sun, X. Wang, Q. Zhang and Z. Zou, *Chin. J. Catal.*, 2021, **42**, 164–174.
16 Y. Li, M. Zhang, L. Zhou, S. Yang, Z. Wu and Y. Ma, *Acta Phys.-Chim. Sin.*, 2021, **37**, 1–17.
17 X. Dong, S. Wang, Q. Wu, K. Liu, F. Kong and J. Liu, *J. Alloys Compd.*, 2021, **875**, 166032.
18 K. Pandi, S. K. Lakhera and B. Neppolian, *Mater. Lett.*, 2021, **303**, 130467.
19 J. Li, Y. Wang, X. Li, Q. Cao and S. Zhang, *J. Alloys Compd.*, 2021, **881**, 160551.
20 P. An, Y. Fu, D. Wei, Y. Guo, W. Zhan and J. Zhang, *Acta Phys.-Chim. Sin.*, 2021, **37**, 2001025.
21 Y. Yang, C. Zhang, D. Huang, G. Zeng, J. Huang, C. Lai, C. Zhou, W. Wang, H. Guo, W. Xue, *et al.*, *Appl. Catal., B*, 2019, **245**, 87–99.
22 H. Zhao, S. Sun, P. Jiang and Z. J. Xu, *Chem. Eng. J.*, 2017, **315**, 296–303.

23 Y. Yang, F. Li, W. Li, W. Gao, H. Wen, J. Li, Y. Hu, Y. Luo and R. Li, *Int. J. Hydrogen Energy*, 2017, **42**, 6665–6673.
24 M. W. Kadi, R. M. Mohamed, A. A. Ismail and D. W. Bahnemann, *Appl. Nanosci.*, 2020, **10**, 223–232.
25 Y. Li, S. Zhu, Y. Xu, R. Ge, J. Qu, M. Zhu, Y. Liu, J. M. Cairney, R. Zheng and S. Li, *Chem. Eng. J.*, 2020, **421**, 127804.
26 Z. Liang, R. Shen, Y. H. Ng, P. Zhang, Q. Xiang and X. Li, *J. Mater. Sci. Technol.*, 2020, **56**, 89–121.
27 X. Zong, J. Han, G. Ma, H. Yan, G. Wu and C. Li, *J. Phys. Chem. C*, 2011, **115**, 12202–12208.
28 R. Shen, D. Ren, Y. Ding, Y. Guan, Y. H. Ng, P. Zhang and X. Li, *Sci. China Mater.*, 2020, 1–36.
29 J. Yu, Y. Yu, Z. Peng, X. Wei and C. Bei, *Appl. Catal., B*, 2014, **156–157**, 184–191.
30 Z. Li, Z. Zhang, Z. Dong, Y. Wu and Y. Liu, *J. Solid State Chem.*, 2021, **302**, 122305.
31 R. Shen, J. Xie, P. Guo, L. Chen, X. Chen and X. Li, *ACS Appl. Energy Mater.*, 2018, **1**, 2232–2241.
32 Z. K. Shen, M. Cheng, Y. J. Yuan, L. Pei and Z. Zou, *Appl. Catal., B*, 2021, **295**, 120274.
33 D. Ge, R. Luo, X. Wang, L. Yang, W. Xiong and F. Wang, *Appl. Surf. Sci.*, 2021, **566**, 150639.
34 X. Fei, M. Liu, C. Cheng, J. Deng and J. Shi, *ChemCatChem*, 2018, **10**, 5441–5448.
35 H. Li, M. Wang, Y. Wei and F. Long, *J. Colloid Interface Sci.*, 2019, **534**, 343–349.
36 R. Shen, J. Xie, Q. Xiang, X. Chen, J. Jiang and X. Li, *Chin. J. Catal.*, 2019, **40**, 240–288.
37 Q. Wang, C. Chen, S. Zhu, X. Ni and Z. Li, *Res. Chem. Intermed.*, 2019, **45**, 1–19.
38 R. Shen, W. Liu, D. Ren, J. Xie and X. Li, *Appl. Surf. Sci.*, 2019, **466**, 393–400.
39 F. Chen, H. Yang, X. Wang and H. Yu, *Chin. J. Catal.*, 2017, **38**, 296–304.
40 W. He, H. Dong, P. Zhao, Y. Huang and L. Yu, *J. Alloys Compd.*, 2021, **883**, 160775.
41 X. Wu, D. Li, Y. Huang, B. Chen and W. Shi, *Appl. Surf. Sci.*, 2021, **565**, 150012.
42 G. Bi, J. Wen, L. Xin, L. Wei, J. Xie, Y. Fang and W. Zhang, *RSC Adv.*, 2016, **6**, 31497–31506.
43 L. Kong, Y. Dong, P. Jiang, G. Wang, H. Zhang and N. Zhao, *J. Mater. Chem. A*, 2016, **4**, 9998–10007.
44 D. Tang and G. Zhang, *Appl. Surf. Sci.*, 2017, **391**, 415–422.
45 H. Qin, R. T. Guo, X. Y. Liu, X. Shi, Z. Y. Wang, J. Y. Tang and W. G. Pan, *Colloids Surf., A*, 2020, **600**, 124912.
46 H. Pang, C. Wei, X. Li, G. Li, Y. Ma, S. Li, J. Chen and J. Zhang, *Sci. Rep.*, 2014, **4**, 1–8.
47 M. Wang, M. Shen, L. Zhang, J. Tian, X. Jin, Y. Zhou and J. Shi, *Carbon*, 2017, **120**, 23–31.
48 H. Liu, Z. Jin, Z. Xu, Z. Zhang and D. Ao, *RSC Adv.*, 2015, **5**, 97951–97961.
49 C. Yang, Q. Tan, Q. Li, J. Zhou and K. Lv, *Appl. Catal., B*, 2020, **268**, 118–738.
50 J. Zou, W. Zhou, L. Huang, B. Guo and L. Wu, *J. Catal.*, 2021, **400**, 347–354.
51 G. Zhou, Y. Chen, H. Dong, L. Xu, X. Liu, C. Ge, D. Sun and Y. Tang, *Int. J. Hydrogen Energy*, 2019, **44**, 26338–26346.
52 Z. Sun, M. Zhu, M. Fujitsuka, A. Wang, C. Shi and T. Majima, *ACS Appl. Mater. Interfaces*, 2017, **9**, 30583–30590.
53 T. P. Rugma, A. Watts, V. S. Vijayarajan, S. K. Lakhera and B. Neppolian, *Mater. Lett.*, 2021, **302**, 130292.
54 Y. Mohammad, S. A. Hira, H. Lim, S. Song and H. P. Kang, *J. Mater. Chem. A*, 2021, **14**, 9018–9027.
55 Y. Dong, L. Kong, P. Jiang, G. L. Wang, N. Zhao, H. Zhang and B. Tang, *ACS Sustainable Chem. Eng.*, 2017, **5**, 6845–6853.
56 J. Lin, R. Zhu, D. L. Phillips and J. C. Yu, *Adv. Funct. Mater.*, 2017, **27**, 1703484.
57 L. Wang, C. Zhu, L. Yin and W. Huang, *Acta Phys.-Chim. Sin.*, 2020, **36**, 1907001.
58 Y. Chen, L. Li, Q. Xu, T. Düren, J. Fan and D. Ma, *Wuli Huaxue Xuebao*, 2021, **37**, 2009080.
59 H. Juanjuan, D. H. Du Jianmei, X. Gengsheng and Y. Yupeng, *Acta Phys.-Chim. Sin.*, 2020, **36**, 1905056.
60 H. Xu, R. Xiao, J. Huang, Y. Jiang, C. Zhao and X. Yang, *Chin. J. Catal.*, 2021, **42**, 107–114.
61 T. Zhang, Y. Liu, Y. Rao, X. Li, D. Yuan, S. Tang and Q. Zhao, *Chem. Eng. J.*, 2020, **384**, 123350.
62 S. Samanta, V. R. Battula, N. Sardana and K. Kailasam, *Appl. Surf. Sci.*, 2021, **563**, 150409.
63 J. Zhang, M. Zhang, C. Yang and X. Wang, *Adv. Mater.*, 2014, **26**, 4121–4126.
64 H. Yang, R. Cao, P. Sun, X. Deng, S. Zhang and X. Xu, *Appl. Surf. Sci.*, 2018, **458**, 893–902.
65 P. Senthilkumar, D. A. Jency, T. Kavinkumar, D. Dhayanithi, S. Dhanuskodi, M. Umadevi, S. Manivannan, N. Giridharan, V. Thiagarajan, M. Sriramkumar, *et al.*, *ACS Sustainable Chem. Eng.*, 2019, **7**, 12032–12043.
66 Y. Chen, W. Li, D. Jiang, K. Men, Z. Li, L. Li, S. Sun, J. Li, Z.-H. Huang and L.-N. Wang, *Sci. Bull.*, 2019, **64**, 44–53.
67 F. Mei, Z. Li, K. Dai, J. Zhang and C. Liang, *Chin. J. Catal.*, 2020, **41**, 41–49.
68 M. Song, X. Xu, J. Xie and L. Xin, *Chin. J. Catal.*, 2017, **38**, 1970–1980.
69 Y. Shan, Y. Guo, Y. Wang, X. Du and L. Chen, *J. Colloid Interface Sci.*, 2021, **599**, 507–518.
70 R. Shen, K. He, A. Zhang, N. Li, Y. H. Ng, P. Zhang, J. Hu and X. Li, *Appl. Catal., B*, 2021, **291**, 120104.
71 D. Ren, W. Zhang, Y. Ding, R. Shen, Z. Jiang, X. Lu and X. Li, *Sol. RRL*, 2020, **4**, 1900423.
72 J. Wen, J. Xie, R. Shen, L. Xin, X. Y. Luo, H. Zhang, A. Zhang and G. Bi, *Dalton Trans.*, 2017, **46**, 1794–1802.